Association Aéronautique et Astronautique de France

60th 3AF International Conference on Applied Aerodynamics
23 – 25 February 2026, Paris - France

AERO2026-05

Multi-point shape optimisation of non-axisymmetric nacelles using an adjoint method

H. Lushington [(1)], D. G. MacManus[(1)], F. Tejero[(1)], M. Meyer[(2)] and C. Sheaf[(3)]
[(1)] Cranfield University, Cranfield, Bedfordshire, MK43 0AL, United Kingdom,
Email: henry.lushington@cranfield.ac.uk
[(2)]Rolls-Royce Deutschland Ltd & Co KG, D-15827 Blankenfelde-Mahlow, Germany
[(3)] Rolls-Royce plc., P.O. box 31, Derby, DE24 8BJ, United Kingdom

ABSTRACT

Ultra-High Bypass Ratio (UHBR) aero-engines can provide specific fuel consumption benefits at the expense of potential increases in powerplant weight and drag. Designing compact nacelles through computational optimisation methods has been a way to reduce such penalties. This paper presents an adjoint optimisation framework that is used for the multi-point design of compact aero-engine nacelles at cruise and windmilling diversion conditions. A B-Spline morphing method is used to deform the nacelle geometry using surface control points. Fully viscous Computational Fluid Dynamics (CFD) calculations alongside an adjoint solver allow optimisation of the powerplant Net Propulsive Force (NPF_D) or Net Vehicle Force (NVF_D) through a gradient-based algorithm. Weighting factors were used to generate a Pareto front between the two operating conditions. Overall, the developed framework was successful in designing compact nacelles for cruise and diversion conditions. Additionally, the method was able to reduce computational cost by up to 8-fold for isolated configurations and by an estimated factor of about 300 for installed configurations compared to the previous state of the art. This demonstrates the potential viability of the adjoint framework for application during early stages of industrial design.

1. INTRODUCTION

The desire to reduce aviation related emissions has led to increased interest and research on Ultra-High Bypass Ratio (UHBR) engines with Bypass Ratios (BPR) > 13 [1]. The increase in BPR often leads to a reduced fan pressure ratio which can increase the engine propulsive efficiency and decrease specific fuel consumption [2]. To achieve a greater BPR, designs tend to use larger fan diameters [3] which often leads to increased engine nacelle size and a subsequent increase in overall powerplant weight and drag [3-4]. Compact nacelles may be a way to offset this penalty, with such designs aiming to reduce both the nacelle length and diameter [5]. As a result, however, the aerodynamic performance of the nacelle becomes sensitive to smaller changes in the geometry relative to legacy designs [6]. This is especially apparent at off-design conditions such as take-off and windmilling [7] and it is therefore necessary to include these conditions earlier in the design stage.

Current methods for isolated nacelle optimisation often use global genetic optimisation algorithms with CFD to assess design performance. Several studies have been performed to optimised axi-symmetric nacelles [5][8-9]. These methods have been extended to include 3D effects by optimising non-axisymmetric nacelles at multi-point conditions. Fang *et al.* [10] optimised a non-axisymmetric nacelle with 20 Degrees of Freedom (DoF) using a hybrid genetic algorithm. The study aimed to minimize nacelle drag with a Reynolds-Averaged Navier-Stokes (RANS) Computational Fluid Dynamics (CFD) and thrust-drag bookkeeping (TDBK) approach. Two incidence conditions were used in the optimisation: 0° and 4°. Overall, there was a predicted reduction in nacelle drag of 1.5% at 0° and 4% at 4°. Tejero et al. [11] conducted multi-point optimisation of a non-axisymmetric isolated nacelle using the Non-dominated Sorting Genetic Algorithm II (NSGA-II) algorithm. An intuitive Class Shape Transform (iCST) parameterization was used with 5 aerolines and 20 total geometric DoF. To assess design performance, RANS CFD was performed with an implemented standard TDBK approach. Three optimisation objective functions were considered: 1) the nacelle cruise drag, 2) the nacelle cruise spillage drag and 3) the cruise Mach rise drag. Overall, the study showed the success in evaluating the design space with such a method but highlighted the high computational cost. The paper further explored the use of surrogate models. Here the initial design set of experiments and the first two generations of the optimisation use full RANS CFD calculations. This data then trains the surrogate model which is used for the final generations until the optimisation converges. Overall, this approach yielded a 65% reduction in compute cost within a 5% uncertainty target relative to a full RANS CFD-in-the loop framework. Tejero *et al.* [12] further extended the RANS CFD-in-the-loop framework to optimise nacelles in an installed configuration. Multi-fidelity and dimensionality reduction techniques were employed to reduce computational cost. The iCST parameterisation was used to generate the powerplant geometry with 32 design variables chosen for the optimisation. The aim was to optimise the aircraft Net Vehicle Force (NVF_D) at a mid-cruise condition with the optimisation yielding an overall 0.65% benefit to NVF_D. The result highlighted the importance of optimising nacelles in an installed configuration as the close proximity of the wing to the nacelle trailing edge causes a noticeable change in aerodynamics compared to the isolated configuration.

For this study a multi-point optimisation is conducted that considers the mid-cruise and diversion windmilling condition. The windmilling condition is used to represent an engine-out scenario where there is a significant reduction in the engine Mass Flow Capture Ratio (MFCR). As the engine inlet streamtube shrinks in diameter the flow spillage around the nacelle cowl increases which leads to increased flow acceleration around the cowl lip. The result of this is a strong shock at the leading edge of the cowl which can cause a shock induced boundary layer separation [13]. If separation occurs the nacelle drag often increases between 5-10% at the off-design condition compared to a design with attached flow [7]. Swarthout et al. [13] conducted an optimisation considering both cruise and windmilling diversion conditions. The study used the OMOPSO particle swarm algorithm with a RANS CFD-in-the-loop method. Three frameworks for the windmilling condition were considered: 1) Full regression based on nacelle drag 2) Combined classification and regression based on nacelle drag 3) Classification only. The classification criterion removed designs where the separation length was greater than 5% of the nacelle length. Many of the cruise optimum designs were removed due to the separation criterion. This highlights the need to include the diversion windmilling conditions within the design process as it is a limiting factor for the extent in which the cruise performance can be optimised.

The current state of the optimisation methods for designing non-axisymmetric nacelles in an isolated configuration are limited by computational cost. This is due to the high number of CFD evaluations required by the genetic algorithms. To successfully implement such methods at an early point within an industrial design stage a more time efficient method is needed. Gradient-based optimisation methods present a possible solution as the computational cost can be an order of magnitude smaller compared to gradient-free optimisation. The difficulty comes from calculating the required gradient information. Methods such as finite differencing limit the computational benefit as they require a large number of CFD evaluations. Alternatively, an adjoint method can be used. This calculates the gradient-information of the cost-function with respect to the design variables at the rough cost of one (1) CFD evaluation. The result is that the computational cost is independent to the number of design variables used within the optimisation. In recent years the adjoint approach has been used for powerplant design. Lamkin et al. [14] assessed the application of adjoint aero-propulsive optimisation for an isolated powerplant. The paper studied optimising a high bypass ratio engine to improve Thrust Specific Fuel Consumption (TSFC). A one-dimensional cycle model was coupled to the optimisation. The nacelle, core and plug geometries were optimised, along with the fan force and core inflow and outflow pressure and temperature variables. Overall, the optimisation yielded approximately a 45% reduction in TSFC, although it was observed that the coupled nature of the optimisation presenting a challenge for convergence. While this study looked at aero-propulsive coupled optimisation it did not consider off design conditions, non-axisymmetric nacelles or the effect of the airframe geometry.

The aim of this study is to assess the feasibility of adjoint design for the aerodynamic shape optimisation of non-axisymmetric isolated nacelles. Both cruise and diversion windmilling conditions will be considered in a multi-point approach. Additionally, this paper assesses the application of the optimisation method for the design of a non-axisymmetric nacelle in an installed configuration at cruise conditions.

2. METHODOLOGY

2.1 Methodology overview

An adjoint optimisation framework has been developed within the Computational Fluid Dynamics (CFD) solver STAR-CCM+ [15] to design isolated aero-engine nacelles. This framework consists of geometry morphing of the individual aerolines using a deformative B-Spline method. An unstructured grid is automatically generated and the primal RANS based flow field is calculated. Performance values of interest are extracted and when required the adjoint gradients are calculated. This is passed to the Sequential Quadratic Programming (SQP) gradient-based algorithm which is used to maximise the powerplant Net Propulsive Force (NPF_D).

2.2 Baseline geometry definition

The baseline engine geometry was generated using an in-house tool [16]. This tool creates the intake, cowl and exhaust geometry definitions through the use of intuitive Class Shape Transform functions [16]. These curves make up individual aerolines for the engine (Fig. 1) with five azimuthally equi-spaced aerolines used to generate a 3D half model of the powerplant (Fig. 2). The baseline geometry is a compact nacelle ($L_{nac}/r_{hi} = 3.1$) that has previously been designed through an in-house global optimisation process [7]. This optimisation process used a particle swarm algorithm to optimise for cruise nacelle drag, cruise Mach rise nacelle drag and diversion windmilling nacelle drag. A classification criterion was used to ensure designs at windmilling diversion and End of Runway (EoR) conditions had a separation length below 5% of the nacelle length: $L_{sep}/L_{nac} < 0.05$. The down selected design from this previous study was based on the minimum achieved cruise nacelle drag that did not penalise the off-design conditions. The design also met the separation length criteria. In this regard the baseline design used for this study has already been optimised for the cruise and diversion conditions and so presents a good starting point for the optimiser.

2.3 Geometry morphing

Nacelle cowl morphing was performed using the CAD functionality within STAR-CCM+ [15]. The included Freeform Surface Modelling (FFM) tool is used to fit a B-Spline surface to the cowl. User-defined control points can then be placed on the B-Spline surface with the displacement of these points then smoothly deforming the geometry. Within the scope of this work the FFM approach was applied to the nacelle surface only. A tangential constraint with the intake surface was placed at the cowl leading edge and a fixed boundary constraint was placed at the trailing edge. Surface control points were placed along aerolines that were equi-spaced between 0°and 180° azimuthally (Fig. 2). Two configurations, comprising five and nine aerolines, respectively, were considered for this study. Each aeroline was split into 13 sections with l_i/l_{arc} varying between 0.08 and 0.23. Five surface control points were positioned per aeroline with a slight bias towards the leading edge and point of nacelle maximum thickness (Fig. 3). This slight bias gives increased geometrical control in the area where shock waves form at cruise and diversion conditions. Each point was constrained to move normal to the surface. This approach was chosen as it provided the most robust implementation of the FFM method. To ensure the morphing did not result in excessive changes to the cowl the range bounds set for

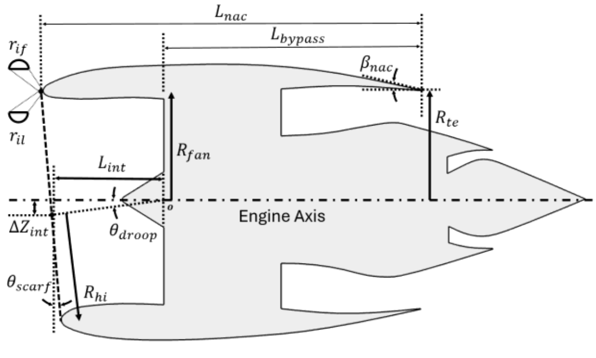

Figure 1: Nacelle parametric term definitions

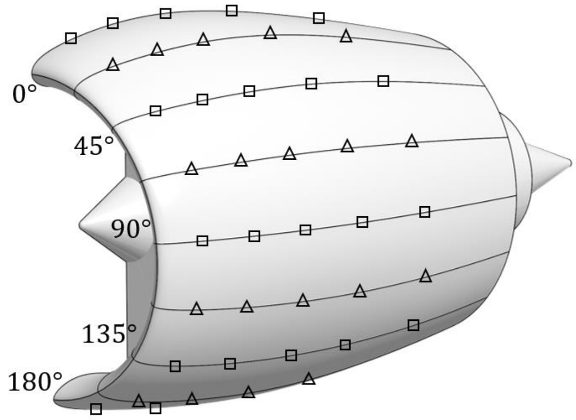

Figure 2: Surface point location on the nacelle cowl surface. Squares represent the 25DoF configuration. Squares and triangles represent the 45DoF configuration.

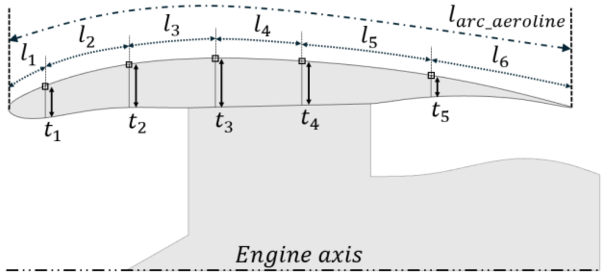

Figure 3: Surface point location along each aeroline with the local thickness line.

the control point movement were based on the local thickness of the nacelle (Fig. 3). This thickness was calculated at the axial location of each control point for each aeroline. The maximum and minimum value of the control point normal displacement was set at $\pm 10\%$ of the local thickness t_i. In total, the two configurations comprised 25 geometric Degrees of Freedom (DoF) for five aerolines and 45 geometric DoF for nine aerolines.

2.4 Computational simulation methodology

At each design iteration, an unstructured polyhedral mesh is automatically generated within a hemispherical domain with a radius of $80r_{max}$ [7]. A grid convergence was performed using four mesh sizes (1.6×10^6, 3.5×10^6, 9.4×10^6, 35×10^6). For each mesh the prism layer, surface and volume growth rates were fixed at 1.2, 1.1 and 1.1. Additionally, the near wall cell height was set to achieve a $y^+ < 50$. This ensures the log law relation is used for the near wall cells. The Grid Convergence Index (CGI) for the 3.5×10^6 cell mesh was 2.6% for the powerplant Net Propulsive Force (NPF_D) parameter. This mesh was chosen for its good trade-off between mesh fidelity and computational cost.

A density-based fully coupled Reynolds-Averaged Navier-Stokes (RANS) solver was used to calculate the powerplant performance metrics. An implicit second order upwind scheme was applied with the Spalart-Allmaras (SA) turbulence model as it is fully differentiable in the adjoint solver. Fluid viscosity was calculated with Sutherland's law [17]. For the adjoint calculation, the GMRES linear solver with defect correction was utilized. The computational domain consists of a freestream pressure boundary condition at the farfield, where the freestream static pressure, temperature and Mach number are prescribed. At the engine fan face, a pressure outlet with a specified mass flow is applied to achieve the desired Mass-Flow Capture Ratio (MFCR). Stagnation inlet conditions are imposed for the bypass and core inlets, with total pressure and temperature set to achieve the target Fan Nozzle Pressure Ratio (FNPR) and Core Nozzle Pressure Ratio (CNPR). Boundary condition values are defined for both a mid-cruise and windmilling diversion condition.

2.5 Thrust and drag accounting

To analyse powerplant performance a Thrust-Drag Bookkeeping (TDBK) approach has been integrated into STAR-CCM+. The thrust and drag domains are split according to the pre-entry and post-exit stream tubes (Fig. 4). These stream tubes capture the flow entering and exiting the engine. The forces acting internally of these stream tubes are classed in the thrust domain whereas forces acting externally are in the drag domain. Forces acting downstream along the drag vector are considered positive. Surface forces denoted by θ consist of the pressure and viscous terms integrated across the surface. For the gauge forces denoted by F that act across boundaries such as the fan, bypass, core, and farfield, the force is calculated as the integral of the pressure and momentum terms. As the stagnation point at the intake lip is unknown and difficult to locate, the modified near-field method [18] is used to calculate the modified nacelle drag (D^*_{nac}) (Eq. 1). This represents the force acting in the drag domain. The internal stream tube forces from the exhaust can be used to calculate the modified Gross Propulsive Force in the drag axis, denoted by the subscript D, (GPF^*_D) (Eq. 2) which represents the force in the thrust domain. The force balance between D^*_{nac} and GPF^*_D can be utilised to determine the overall Net Propulsive Force (NPF_D) (Eq. 3) of the powerplant where an increase in NPF_D is beneficial and can ultimately be exploited to reduce fuel burn.

$$D^*_{nac} = -F_{G0} + \theta_{intk} + \theta_{spin} + F_{G2} + \phi_{nac} \quad (1)$$

$$GPF^*_D = F_{G5} + F_{G13} - (\theta_{bp} + \theta_{cd} + \theta_{cc} + \theta_{pg}) \quad (2)$$

$$NPF_D = GPF^*_D - D^*_{nac} \quad (3)$$

2.6 Optimisation overview

A Sequential Quadratic Programming (SQP) algorithm [20] is used for the optimisations. For the isolated configuration the cost function is taken as a combination of the normalised NPF_D (C_{NPF_D}) (Eq. 6) at cruise and diversion conditions (Eq. 4), where $C_{NPF_D} > 1$ represents a benefit to NPF_D compared to the baseline. Weighting variables w_{cruise} and w_{div} (Eq. 5) are utilized to control the influence of the operating points on the optimisation.

$$f(x) = w_{cruise} C_{NPF_D cruise} + w_{div} C_{NPF_D div} \quad (4)$$

$$w_{cruise} + w_{div} = 1 \quad (5)$$

$$C_{NPF_D} = NPF_D / NPF_D^{baseline} \quad (6)$$

3. RESULTS

3.1 Multi-point optimisation for isolated powerplant nacelle

A total of five weighting values between 0 and 1 were used for the multi-point optimisations (Tab. 1). This

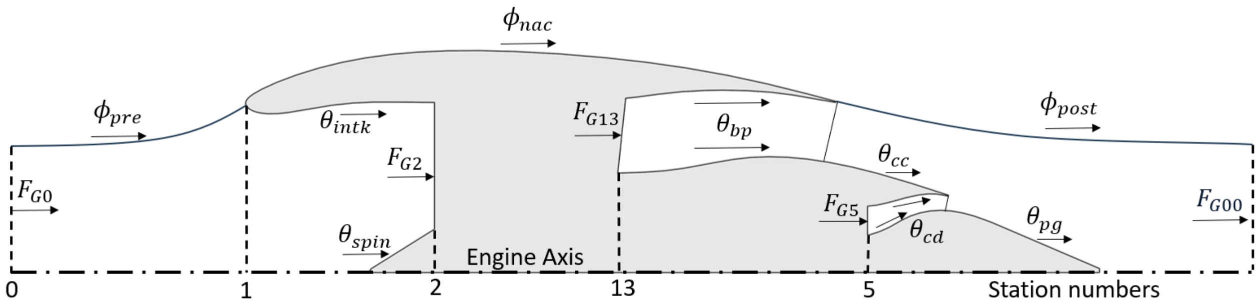

Figure 4: Thrust-Drag Bookkeeping method and terminology used to evaluate the Net Propulsive Force. Based on [19].

resolves the Pareto front such that the general trends can be seen without unnecessary computational expense.

Table 1: Weighting values and naming scheme used for multi-point optimisations.

Optimisation name	w_{cruise}	w_{div}
0.0C, 1.0D	0%	100%
0.25C, 0.75D	25%	75%
0.5C, 0.5D	50%	50%
0.75C, 0.25D	75%	25%
1.0C, 0.0D	100%	0%

The influence of dimensionality on the optimised designs is limited. Differences between the 25DoF and 45DoF configurations along the Pareto front are most pronounced for the diversion dominant design (0.0c,1.0d), where the absolute differences in NPF_D between the dimensionalities are approximately 2% in NPF_{D_cruise} and 1.5% in NPF_{D_div} (Fig. 8). The most notable geometric variation between the two configurations (25Dof and 45DoF) occurs for the cruise dominant designs (1.0c,0.0d), where the 45DoF case exhibits a more pronounced reduction in nacelle fore-section thickness between 90° and 180° azimuthally compared to the 25DoF case. Additionally, the dimensionality influences the computational cost relative to previous gradient-free methods for isolated nacelle optimisation. A simple estimate indicates that the adjoint approach yields 8-fold and 15-fold reductions in computational cost for the 25DoF and 45DoF cases, respectfully, compared to a gradient-free method. The difference in computational benefit between 25DoF and 45DoF is because the adjoint method scales better with dimensionality compared to a gradient-free method [24].

The Pareto front exhibits an exponential type of behaviour (Fig. 8), similar to that reported by Swarthout *et al.* [13]. This is characterised by almost a straight line for the diversion dominant optimisations (0.0c,1.0d; 0.25c,0.75d; 0.5c,0.5d) in which the NPF_{D_div} benefit remains relatively constant while the performance at the cruise condition is penalised. Then, as the optimisation becomes more cruise dominated (0.75c,0.25d; 1.0c,0.0d) there is a sharp decrease in diversion performance with a reduction in NPF_{D_div} and an increase in cruise performance with a benefit to NPF_{D_cruise} (Fig. 8). A detailed assessment of the aerodynamic characteristics and the effect on NPF_D for the 45 DoF case is discussed further on in section 3.1.

Two conclusions can be drawn from the Pareto front. First, as the weightings move towards the diversion condition there is minimal benefit to NPF_{D_div} and a large penalty to NPF_{D_cruise}. This suggests there is little justification to use weightings with $w_{div} > 50\%$ as the design point cruise performance is penalised with no noticeable gain to off-design performance. Second, the region of optimal robust designs is evident when using cruise dominated weightings ($0.75 < w_{cruise} < 1.0$) in which the NPF_{D_cruise} performance is maximised while ensuring adequate diversion performance.

The baseline design is located on the adjoint Pareto front (Fig. 8). As previously mentioned, the provenance of this design is from an already established global optimisation framework [7] in which the nacelle drag at cruise, diversion windmilling and cruise Mach rise were minimized. A design taken from that study was used as the baseline for the adjoint optimisations. This design was taken as the minimum cruise, diversion and cruise Mach rise drag while ensuring off-design performance met a separation length classification. This classification ensures that the separation length does not exceed 5% of the nacelle length. As the baseline matches closely with the adjoint Pareto front the two independent optimisation methods show an agreement on the nacelle performance between the cruise and diversion windmilling condition.

Overall, NPF_{D_cruise} is increased by 0.54% for the cruise dominant design with 45 DoF (45DoF; 1.0c,0.0d) relative to the baseline. This design has a reduced fore-body thickness relative to the baseline (Fig. 5) which increases

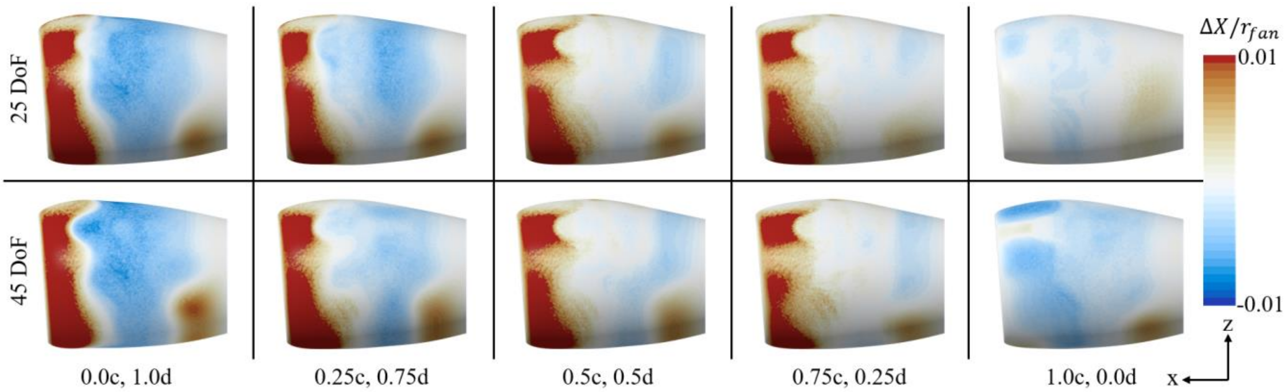

Figure 5: Geometry difference between optimised and baseline geometry normalised with the fan radius. Values are positive where the optimised geometry is thicker than the baseline, negative where the optimised geometry is thinner than the baseline. Both Degrees of Freedom (DoF) are shown for all multi-point weightings (c – Cruise, d - Diversion)

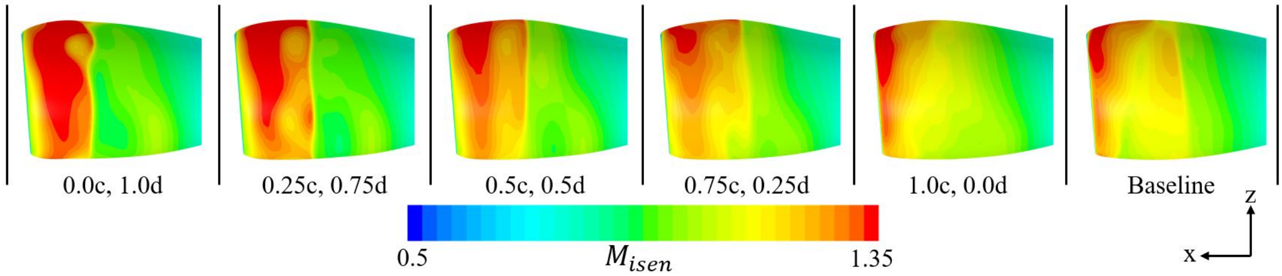

Figure 6: Isentropic Mach number contour plots for the optimised and baseline designs at the cruise condition. Shown for the 45DoF configuration only. All multi-point weightings shown (c - Cruise, d – Diversion)

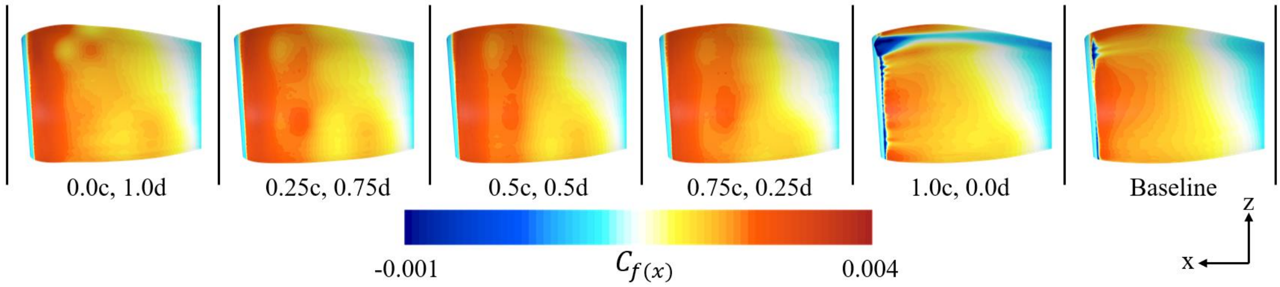

Figure 7: Skin friction coefficient (x-component) contour plots for the optimised and baseline designs at the diversion condition. Shown for the 45DoF configuration only. All multi-point weightings shown (c - Cruise, d – Diversion)

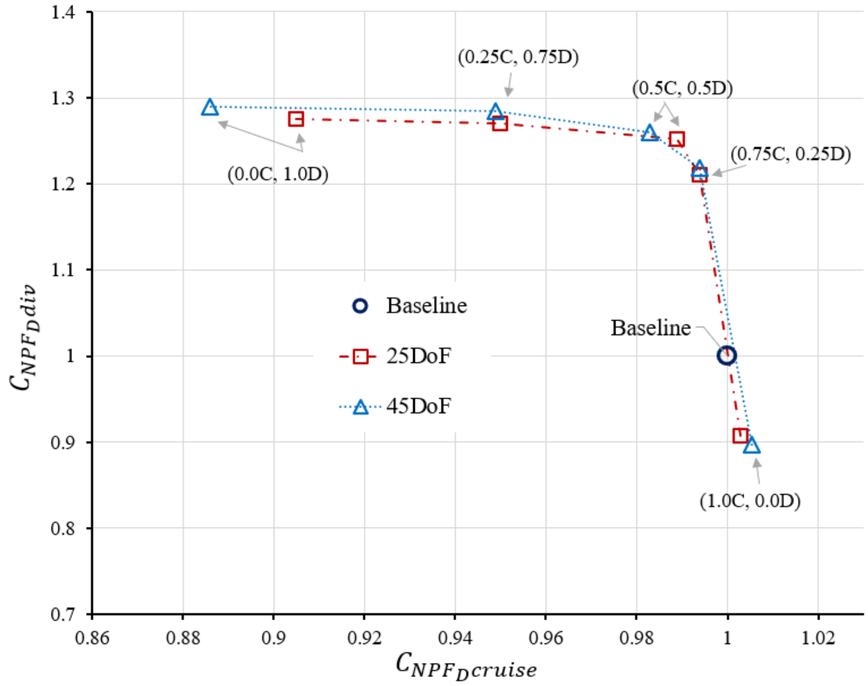

Figure 8: Pareto front generated from adjoint multi-point optimisations between cruise Net Propulsive Force ($C_{NPF_D cruise}$) and diversion Net Propulsive Force ($C_{NPF_D div}$). Both 25 and 45 Degree of Freedom (DoF) cases are shown. All multi-point weightings shown (c – Cruise, d - Diversion)

the curvature, and consequently the flow acceleration, over the leading edge. At the cruise condition, this increased flow acceleration produces a stronger shock on the cruise dominant design (45DoF; 1.0c,0.0d) that is positioned further forward in the axial direction compared to the baseline (Fig. 6). The resulting increase in forward loading improves the pressure recovery between the shock and the nacelle trailing edge, thereby reducing the pressure-gradient force between the nacelle fore and aft sections.

At the diversion condition, this design (45DoF;1.0c,0.0d) has approximately a 10% reduction in NPF_{D_div} relative to the baseline. At this diversion condition the Mass Flow

Capture Ratio (MFCR) is reduced relative to the cruise condition which results in a decreased streamtube radius. This increases the local incidence angle at the nacelle leading edge which results in the formation of a strong shock. For the cruise dominant optimization design (45DoF;1.0c,0.0d) assessed at the diversion condition, the reduction in fore-body thickness relative to the baseline (Fig. 5) increases the shock strength at the leading edge which causes a shock-induced boundary layer separation (Fig. 7) and an overall penalty in NPF_{D_div}.

As the optimisation weightings shift towards being more diversion dominated (0.25c,0.75d; 0.0c,1.0d) the nacelle forebody is thickened near the leading edge, while the nacelle mid-to-aft section is progressively thinned with increasing w_{div} (Fig. 5). These geometry changes move the position of maximum thickness (r_{max}) axially forwards towards the leading edge. For the diversion-dominant design with 45DoF (45DoF; 0.0c,1.0d) the increased thickness of the nacelle forebody reduces the leading-edge curvature, decreasing the shock strength at the diversion condition relative to the baseline. Additionally, at the diversion condition, the thinning of the nacelle aft section for this design (45DoF; 0.0c,1.0d) improves the pressure recovery between the shock and the nacelle trailing edge. Overall, the pressure drag is reduced and there is a beneficial increase in NPF_{D_div} of 29% for the diversion dominant design (45DoF; 0.0c,1.0d) relative to the baseline. At the cruise condition, the forward shift of r_{max} for the diversion dominant design (45DoF; 0.0c,1.0d) moves the shock axially rearward towards the trailing edge (Fig. 6). This reduces the forward loading and NPF_{D_cruise} is decreased by approximately 11.5% for the diversion dominant design (45DoF; 0.0c,1.0d) relative to the baseline.

3.2 Installed single-point optimisation

While isolated compact nacelles can be designed with current state-of-the-art methods, the optimisation of a coupled powerplant and airframe configuration brings additional challenges. When powerplants are installed in a close-coupled position with the airframe the potential benefits found in the isolated configuration can diminish by up to a factor of three [21]. This is due to adverse installation effects between the inboard side of the nacelle and the airframes lower wing surface. It is therefore pertinent to explore the optimisation of compact nacelles in an installed configuration in addition to an isolated configuration. For this reason, the established isolated adjoint optimisation capability has been extended to the single-point optimisation of a coupled powerplant airframe configuration.

The installed single-point optimisation follows the same CFD approach used for the isolated configuration. The mesh consists of a polyhedral surface and volume grid with a 3000m farfield, which is specified in the Drag Prediction Workshop 6 [22]. Wall functions were used to minimise cell count and improve adjoint convergence. First cell heights were specified separately for each geometry section to achieve y^+ values between 50-100. This ensured near wall cell aspect ratios were not too large – something that can negatively affect adjoint convergence. Five mesh sizes were generated ($116 \times 10^6, 76 \times 10^6, 54 \times 10^6, 37 \times 10^6, 25 \times 10^6$) to assess the grid convergence. The 37×10^6 mesh was chosen as it was deemed the largest usable cell size within the timeframe of this study. It has a CGI of 5.8% which is higher than what would be desirable, but this would still allow an initial proof of the method. The final optimised results are assessed with a wall resolved mesh to evaluate the effect of the coarse mesh.

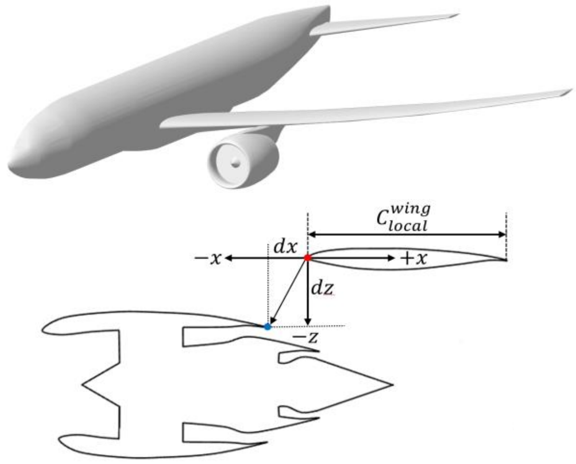

Figure 9: Top: Coupled powerplant airframe configuration. Bottom: Engine installation position definition [21]

The Net Vehicle Force (NVF_D) metric (Eq. 7) was used as the objective function to be maximised as it includes the powerplant NPF_D and the airframe drag ($D_{a/f}$), both of which are inherently coupled to changes in the nacelle surface. Additionally, an increase in NVF_D along the drag axis, denoted by subscript D, is beneficial and closely related to the total aircraft fuel burn. To ensure the aircraft remained trimmed a lift constraint of $C_L = 0.5 \pm 0.001$ was applied through a hill climbing algorithm (Eq. 8-10) which was used to step the angle of attack during the primal simulations.

$$NVF_D = NPF_D - D_{a/f} \tag{7}$$

$$\alpha_{i+1} = \alpha_i + \Delta\alpha \tag{8}$$

$$\Delta\alpha = \frac{-R_{C_L}}{C_{L_{Target}}} \tag{9}$$

$$R_{C_L} = C_{L_i} - C_{L_{Target}} \tag{10}$$

The geometry used for the airframe is the full-scale wing-body-tail Common Research Model (CRM) configuration from the Drag Prediction Workshop 4 (DPW-4) [23]. The powerplant baseline geometry is mounted in an under-wing configuration in a coincident position ($dx/C_{local}^{wing} = 0$) at 15% down ($dz/C_{local}^{wing} = 0.15$) relative to the wing local chord (Fig. 9). The installation angles are taken from the CRM baseline where the toe angle $\theta_{toe} = 2.25°$ and the pitch angle $\theta_{pitch} = 1.75°$ [23]. The baseline powerplant is the same as the one used in the isolated optimisations. However, the geometry now includes the pylon which is also created through a previously developed iCST parameterisation [16].

The STAR-CCM+ Freeform Surface Modelling (FFM) tool [15] was used to morph the nacelle cowl using surface control points. The full azimuthal range of the nacelle was included using 16 equi-spaced aerolines spanning 0° and 360° azimuthally (Fig. 10). Five control points were placed along each aeroline, consistent with the isolated optimisation configuration (Fig. 3). For the top aeroline at 0°, only the first two control points were used due to the pylon. With the installed nacelle, the FFM tool was observed to introduce inflection points along the aerolines. To mitigate this, the displacement of each control point i was smoothed through a Gaussian function. This smoothing was based on the displacment of neighbouring points along the same aeroline (Eq. 11). The constant ε was manually set for each point to ensure smooth geometry without any wavy charecteristics.

$$\Delta x_i = \Delta x_i + \Delta x_{i-1} e^{-(\varepsilon_{i-1})^2} + \Delta x_{i+1} e^{-(\varepsilon_{i+1})^2} \qquad (11)$$

In the installed configuration the baseline geometry exhibits a region of increased isentropic Mach number towards the inboard aft-section of the nacelle (Fig. 11) when compared to the isolated baseline (Fig. 6). This is due to the proximity of the nacelle surface to the wing leading edge where there is a large region of high pressure. The characteristics of the flow on the outboard section (Fig. 11) are similar to the baseline in the isolated configuration (Fig. 6) with a double shock present.

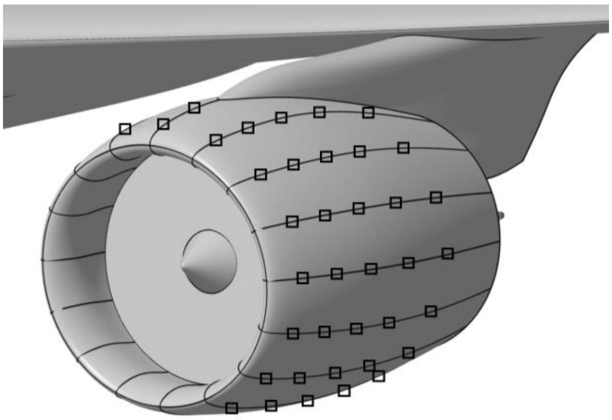

Figure 10: Surface control point placement across the installed nacelle surface

The installed force values have been normalized with the standard net thrust of the engine F_N which is in the order of 60kN [7]. This is to approximately relate the force changes to overall engine fuel burn. All reported results are with a wall resolved mesh. On the inboard section the baseline nacelle is already forward loaded with the shock close to the leading edge (Fig. 11). With the optimised design the main change occurs in the nacelle mid to aftbody, specifically between the 0° and 90° azimuthal angles. Here, the isentropic Mach number is reduced relative to the baseline (Fig. 11), leading to an increase in static pressure. As a result, there is a decrease in pressure-gradient force and subsequent pressure drag. A similar mechanism occurs on the outboard section; it is most prevalent between the 90° and 180° azimuthal angles, where the isentropic Mach number decreases relative to

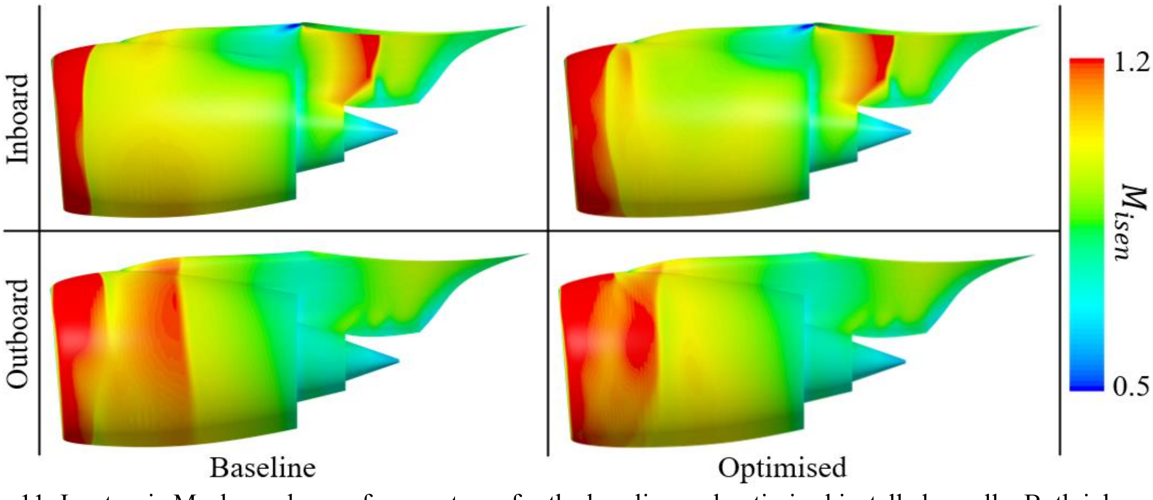

Figure 11: Isentropic Mach number surface contours for the baseline and optimised installed nacelle. Both inboard and outboard sections are shown.

the baseline (Fig. 11). The net result is a 0.62% increase in normalised NVF_D relative to the baseline (Fig. 12).

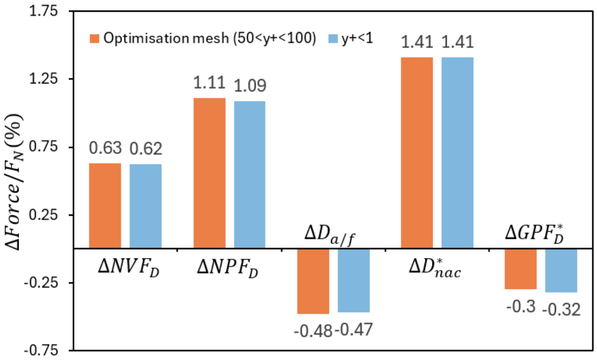

Figure 12: Force breakdown of change in NVF_D of optimised design relative to baseline design for the wall resolved mesh and wall function mesh.

When decomposing the NVF_D value into its constituent parts (Fig. 12) there is a penalty to the exhaust Gross Propulsive Force (GPF^*_D) of 0.3% but an overall net benefit to the Net Propulsive Force (NPF_D) of 1.09% (Fig. 12) by optimising the nacelle. Additionally, by improving the aerodynamic characteristics of the nacelle the airframe drag ($D_{a/f}$) is penalised by 0.47% which is caused by an increase in wing drag from the installation effects. This highlights the importance of optimising the nacelle with a coupled powerplant and airframe configuration. Additionally, the wall function mesh has proven to be accurate when predicting the change in force between two installed nacelle designs. The maximum difference in $\Delta Force/F_n$ was 0.02% between the wall function mesh and the wall resolved mesh (Fig. 12). To assess the computational benefit of the adjoint method for installed nacelle optimisation a simple estimate of the computational time for an equivalent gradient free method has been considered. Overall, it is estimated that the installed adjoint approach has an approximate 300-fold reduction in computational cost relative to a previous gradient-free method. The larger reduction in computational cost for the installed optimisation (300-fold) compared to the isolated optimisation (8-fold with 25DoF) is due to two factors. First, adjoint optimisations scale more favourably with problem dimensionality than gradient-free methods [24], making the increased dimensionality of the installed case (77DoF) more costly for gradient-free methods relative to the isolated case (25DoF). Second, the installed case involves a single-point optimisation while the isolated case requires five separate multi-point optimisations; this is compared to the one (1) gradient-free optimisation that is needed for the isolated case. This means the adjoint method scales more effectively for the installed case.

4. CONCLUSION

This paper presents a multi-point adjoint optimisation framework for the design of isolated compact nacelles. The framework has also been extended to the single-point optimisation of nacelles in a coupled powerplant and airframe configuration. Overall, the contribution of this paper is in the demonstration of the adjoint method applied to multi-point isolated nacelle design. The developed framework has proven to be viable for the generation of a Pareto front between cruise and diversion conditions for the design of isolated nacelles. Extending this framework to design nacelles in a coupled powerplant and airframe configuration has also proven successful with an achieved 0.62% beneficial increase in Net Vehicle Force (NVF_D) relative to the baseline. This is closely related to a similar reduction in cruise fuel burn. Additionally, a contribution of the study is the assessment of the computational benefits of the adjoint method for isolated and installed nacelle design. The framework provided a computational cost reduction of 8-fold and 15-fold for the isolated case with 25 Degrees of Freedom (DoF) and 45 DoF, respectfully, relative to a gradient-free method. Furthermore, the installed case achieved an approximately 300-fold decrease in computational cost relative to the previous state of the art gradient-free method. The findings indicate that the adjoint optimisation method is well suited for application within early-stage industrial design and could potentially help bring more efficient nacelle design to future UHBR aero-engines. Future work will look to extend the coupled powerplant and airframe capability to a multi-point scenario with the inclusion of powerplant bulk parameters such as installation angles. Further to this, a completely parametric geometry tool that can calculate geometric gradients through automatic differentiation is being explored. This will allow for the optimisation of intuitive parameters and the application of geometric constraints on the optimisation.

5. ACKNOWLEDGEMENTS

H. Lushington was supported by the Engineering and Physical Sciences Research Council [grant number EP/Y528535/1], Rolls Royce plc., and Cranfield University.

6. REFERENCES

1. Barbosa, F. (2022) Ultra High Bypass Ratio Engine Technology Review - The Efficiency Frontier for the Turbofan Propulsion. *SAE Technical Paper,* 2021-36-0032.

2. Dankanich, A. & Peters, D. (2017) Turbofan Engine Bypass Ratio as a Function of Thrust and Fuel Flow. *Mechanical Engineering and Materials Science Independent Study,* 34.

3. Suder, K., Delaat, J., Hughes, C., Arend, D. & Celestina, M. (2013) NASA Environmentally Responsible Aviation Project's Propulsion Technology Phase I Overview and Highlights of Accomplishments. *51st AIAA Aerospace Sciences Meeting,* AIAA 2013-414

4. Byerley, AR, Rolling, AJ, & Van Treuren, KW. (2013) Estimating Gas Turbine Engine Weight, Costs, and Development Time During the Preliminary Aircraft Engine Design Process. *ASME Turbo Expo 2013,* Vol 4, V004T08A011

5. Tejero, F., Robinson, M., MacManus, D. & Sheaf, C. (2019). Multi-objective optimisation of short nacelles for high bypass ratio engines. *Aerospace Science and Technology,* Vol. 91, pp. 410-421,

6. Magrini, A., Buosi, D., Benini, E. & Sheaf, C. (2021). Ultra-high bypass nacelle geometry design space exploration. *AIAA Scitech 2021 Forum*, AIAA 2021-0990

7. Tejero, F., MacManus, D., Matesanz-Garcia, J., Swarthout, A. & Sheaf, C. (2023). Towards the Design and Optimisation of Future Compact Aero-Engines: Intake/Fancowl Trade-off Investigation. *International Journal of Numerical Methods for Heat and Fluid Flow,* Vol.33

8. Li, S. & Zhong, Y. (2016). A Turbofan-Engine Nacelle Shape Design and Optimization Method for Natural Laminar Flow Control. *ASME Turbo Expo 2016,* Vol 1, V001T01A027

9. Albert M. & Bestle D. (2014). Automatic Design Evaluation of Nacelle Geometry Using 3D-CFD. *15th AIAA Multidisciplinary Analysis and Optimization Conference,* AIAA 2014-2039

10. Fang, X., Zhang, Y., Li, S., & Chen. H. (2016). Transonic Nacelle Aerodynamic Optimization Based on Hybrid Genetic Algorithm. *17th AIAA Multidisciplinary Analysis and Optimization Conference,* AIAA 2016-3833

11. Tejero, F., Christie, R., MacManus, D. & Sheaf*, C.* (2021). Non-axisymmetric aero-engine nacelle design by surrogate-based methods. *Aerospace Science and Technology*, Vol. 117

12. Tejero, F., MacManus, D., Hueso Rebassa, J., Sánchez Moreno, F., Goulos, I. and Sheaf, C. (2022). Aerodynamic optimisation of civil aero-engine nacelles by dimensionality reduction and multi-fidelity techniques. *International Journal of Numerical Methods for Heat & Fluid Flow,* 33(4)

13. Swarthout, A., MacManus, D. G., Tejero, F., Matesanz-García, J., Boscagli, L. & Sheaf, C. (2022). A comparative assessment of multi-objective optimisation methodologies for aero-engine nacelles. *33rd Congress of the International Council of the Aeronautical Sciences*

14. Lamkin, A., Yildrim, A & Martins, J. (2022). Coupled Aeropropulsive Analysis and Optimization of a High Bypass Turbofan Engine. *33rd Congress of the International Council of the Aeronautical Sciences*

15. Siemens Digital Industries Software. (2025). Simcenter STAR-CCM+, version 2502.0. Siemens

16. Christie, R., Robinson, M., Tejero, F. & MacManus, D. (2019). The use of hybrid intuitive class shape transformation curves in aerodynamic design. *Aerospace Science and Technology,* Vol. 95

17. Sutherland, W. (1893). The viscosity of gases and molecular force. *The Philosophical Magazine,* Vol. 36, pp. 507-531

18. Stańkowski, T., MacManus, D., Sheaf, C., Christie, R. (2016). Aerodynamics of aero-engine installation. *Proceedings of the Institution of Mechanical Engineers, Part G: Journal of Aerospace Engineering*. 2016;230(14):2673-2692

19. Goulos, I., Otter, J., Tejero, F., Hueso-Rebassa, J., MacManus, D., Sheaf, C. (2021). Civil turbofan propulsion aerodynamics: Thrust-drag accounting and impact of engine installation position. *Aerospace Science and Technology,* Vol. 111

20. Schittkowski, K. (2009). NLPQLP: A Fortran Implementation of a Sequential Quadratic Programming Algorithm with Distributed and Non-Monotone Line Search—User's Guide, version 4.2. *Department of Computer Science, University of Bayreuth*

21. Tejero, F., Goulos, I., MacManus, D. & Sheaf, C. (2020). Effects of Aircraft Integration on Compact Nacelle Aerodynamics. *AIAA SciTech 2020 Forum and Exposition,* AIAA 2020-2225

22. Tinoco, E., Brodersen, O., Keye, S., Laflin, K., Feltrop, E., Vassberg, J., Mani, M., Rider, B., Wahls, R., Morrison, J., Hue, D., Roy, C., Mavriplis, D. & Murayama, M. (2018). Summary Data from the Sixth AIAA CFD Drag Prediction Workshop: CRM Cases. *Journal of Aircraft,* Vol. 55, pp. 1352-1379

23. Vassberg, J., Tinoco, E., Mani, M., Rider, B., Zickuhr, T., Levy, D., Brodersen, O., Eisfeld, B., Crippa, S., Wahls, R., Morrison, J., Mavriplis, D.& Murayama, M. (2010). Summary of the Fourth AIAA CFD Drag Prediction Workshop. *28th AIAA Applied Aerodynamics Conference*

24. Martins, J. R. R. A., & Ning, A. (2021). Engineering Design Optimization. *Cambridge: Cambridge University Press.*